INORGANIC CHEMISTRY FRONTIERS

RESEARCH ARTICLE

View Article Online
View Journal | View Issue

Cite this: *Inorg. Chem. Front.*, 2026, **13**, 4513

High-temperature biferroicity in a chiral 3D hybrid rare-earth-based double perovskite

Li-Ping Wang,†[a,b] Chang-Chun Fan, †[a,c] Zheng-Hui Hu,[a,b] Hong-Fei Zhao,[a,b] Jian-Rong Li *[a,b] and Chao Shi *[a,b]

Received 28th February 2026,
Accepted 28th March 2026

DOI: 10.1039/d6qi00400h

rsc.li/frontiers-inorganic

Recently, switchable physical properties have been discovered in functional hybrid rare-earth perovskites, which have gained greater attention for potential applications. By consciously introducing a dynamic and spherical organic cation, *R*M3HQ (the *R*-*N*-methyl-3-hydroxylquinuclidinium cation), we synthesized a three-dimensional (3D) nitrate-bridged hybrid rare-earth perovskite, $(RM3HQ)_4K_2[Nd(NO_3)_6]_2$ (**1**), possessing a 4-connected LON framework with a 6^6 topological network (Schläfli symbol). Thermal measurements show that **1** undergoes two reversible phase transitions, at around 370 K and 410 K, respectively. Various-temperature single-crystal structural analyses reveal that **1** crystallizes in the polar space group $P2_1$ at 293 K and 390 K, respectively, and in the chiral space group $P6_322$ at 428 K. The phase transitions support dielectric transitions, making **1** a type of switchable dielectric material. More importantly, the symmetry breaking at 410 K shows a ferroelastoelectric transition with the Aizu notation of 622F2. This study constructs a high-performance hybrid rare-earth perovskite and provides highly promising candidate materials for next-generation multifunctional electronic devices.

Introduction

Responsive functional materials with switchable physical properties are currently a research hotspot, as their tunable characteristics hold great promise for next-generation smart devices.[1–5] Among these materials, hybrid perovskites—combining the advantages of organic and inorganic components—have attracted tremendous interest owing to their superior optical, electronic, and magnetic properties, with their structural phase transition behavior being one of their most attractive features.[6–11] Specifically, hybrid perovskites with structural phase transitions—*i.e.*, those exhibiting a switchable dielectric constant, ferroelectricity, and/or ferroelasticity—have emerged as a key research focus, given their potential applications in the smart energy transition and piezoelectric devices.[12–19] However, a critical bottleneck persists in this field: achieving stable multiferroic coexistence at elevated temperatures. This challenge is particularly significant, as high-temperature multiferroics provide broader operational ranges and exhibit enhanced stability under harsh service conditions, which are both essential for advancing their practical implementation.[20–27]

In recent years, organic–inorganic hybrid perovskites have emerged as a promising platform for designing high-temperature multiferroic materials, owing to their tailorable chemical compositions and dynamic structural characteristics.[21,28–35] In these systems, the synergistic interplay between the order–disorder transitions of flexible organic cations and the structural distortion of inorganic frameworks can drive crystallographic symmetry breaking and further induce multifunctional ferroic order, including ferroelectricity and ferroelasticity. Notably, in hybrid double perovskite systems—an important subclass of this family—the rational design of organic cations, combined with the tunable ionic radii and diverse coordination preferences of metal ions, has enabled the successful construction of a series of multifunctional materials.[36–41] For instance, Hu *et al.* integrated ferroelasticity, multiaxial ferroelectricity, and a magnetic response into a single material *via* a chirality-induction strategy;[42] Jia *et al.* reported a rare-earth-based double perovskite with both pronounced ferroelasticity and a high piezoelectric response, which paves the way for its application in energy-conversion devices;[43] and Miao *et al.* developed a 3D hybrid metal halide perovskite multiferroic material with superior ferroelectric, ferroelastic, piezoelectric, and charge transport properties, endowing it with great potential for ferrophotoelectric device applications.[44] These advances collectively

[a]*Jiangxi Province Key Laboratory of Functional Crystalline Materials Chemistry, Jiangxi University of Science and Technology, Ganzhou 341000, Jiangxi Province, P.R. China. E-mail: jrli@fjirsm.ac.cn, 13064147687@163.com*
[b]*Chaotic Matter Science Research Centre, International Institute for Innovation, Jiangxi University of Science and Technology, Nanchang 330000, Jiangxi Province, P. R. China*
[c]*School of Materials Engineering, Jinling Institute of Technology, Nanjing 211169, P. R. China*
†These authors contributed equally to this work.

demonstrate that the ordered arrangement of two distinct metal centers, coupled with organic–inorganic synergy, can effectively regulate and optimize the multifunctional performances of such systems. Nevertheless, most studies to date have focused on hybrid double perovskites with only a single ferroic order, and reports on 3D hybrid perovskites that achieve the stable coexistence of multiple types of ferroic order remain scarce.[4,45–49]

In this work, we report a new 3D hybrid rare-earth double perovskite crystal, $(R\text{M3HQ})_4K_2[Nd(NO_3)_6]_2$ (**1**, $R\text{M}_3\text{HQ}$ = *R*-*N*-methyl-3-hydroxylquinuclidinium), which features a 4-connected LON framework with a 6^6 topological network (Schläfli symbol). It undergoes two thermally induced phase transitions with a high-temperature ferroelectric transition at 410 K, exhibiting prominent ferroelectricity ($P_s \approx 2.7$ μC cm^{-2}) and reversible ferroelasticity, realizing stable ferroelectric-ferroelastic coexistence. Hirshfeld surface analysis reveals that the extensive O–H···O/N–H···O hydrogen-bond network and K–O coordination interactions synergistically afford structural stability and account for the high phase-transition temperature. This work not only presents a new example of high-temperature multiferroics in rare-earth hybrid materials but also demonstrates, through molecular design and crystal engineering, a viable strategy for tuning the multifunctional properties.

Experimental section

Synthesis

All chemicals are commercially available from Aladdin and used directly without further purification.

Synthesis of $(R\text{M}_3\text{HQ})$I. (*R*)-3-Hydroxylquinuclidinium (0.508 g, 4 mmol) and CH_3I (0.710 g, 5 mmol) were added to 50 mL of ethyl acetate and stirred at room temperature. After reacting for 24 hours, a large amount of white powder was formed and filtered. Powdered (*R*M3HQ)I was obtained by drying at 333 K for 30 minutes; yield: 1.04 g, 85.1%, based on (*R*)-3-hydroxylquinuclidinium.

Synthesis of 1. To eliminate the interference of iodide ions in the reaction system, the synthesized (*R*M3HQ)I (1.012 g, 5 mmol) was first reacted with 1.84 mL of HNO_3 (68%, aq., 10 mmol) at room temperature, and iodide ions were oxidized to elemental iodine. Elemental iodine was removed by heating to 363 K until the solution was clear and transparent. A solution of $(R\text{M3HQ})NO_3$ was obtained, which is named the A solution. Then, $Nd(NO_3)_3{\cdot}6H_2O$ (0.877 g, 2 mmol), KCl (0.149 g, 2 mmol), and 1.10 mL of HNO_3 (68%, aq., 6 mmol) were added to 25 mL of deionized water, which was stirred and dissolved to form the B solution. A mixture of A solution and B solution was stirred, and finally, 10 mL of ionized water was added to reduce the crystal precipitation rate and improve the crystal quality. The mixture was filtered and placed on a heating stage at 313 K to remove volatile solvent, and light-purple single crystals were formed over about 3 days and then collected and dried to obtain $(R\text{M3HQ})_4K_2[Nd(NO_3)_6]_2$ with a yield of 71.8% based on $Nd(NO_3)_3{\cdot}6H_2O$.

Element analysis for **1**. Anal. (%) calc.: C, 22.88; H, 3.84; N, 13.34. Found (%): C, 22.84; H, 3.86; N, 13.38 (Table S1).

Physical property characterization

A single crystal was crushed into powder for DSC measurements. The *P*–*E* loop measurements were performed on a single crystal with an area of ~30 mm^2 and a thickness of ~1 mm along the polar axis in the direction of the monoclinic phase [010]. For more information on performance measurements and single-crystal structure determination, see the SI.

Results and discussion

Phase transition properties

The phase purity of **1** was confirmed based on the good consistency between its experimental and simulated PXRD patterns (Fig. S1). TGA analysis indicated that **1** exhibits thermal stability up to 536 K (Fig. S2). Differential scanning calorimetry (DSC) measurements revealed two pairs of reversible endothermic/exothermic peaks during heating–cooling cycles (Fig. 1 and Fig. S3), with phase-transition temperatures of 370/360 K and 410/400 K, respectively, corresponding to thermal hysteresis of 10 K. Entropy changes (ΔS) were calculated from the average enthalpy changes (ΔH) obtained over the whole phase-transition process. Upon heating, $\Delta S_1 \approx 30.6$ J mol^{-1} K^{-1} at 370 K ($N_1 \approx 6.3$, $\Delta S = R{\cdot}\ln N$) and $\Delta S_2 \approx 9.25$ J mol^{-1} K^{-1} at 410 K ($N_2 \approx 1.7$, see Note S1). Both *N* values are much greater than 1, indicating the structural transition of **1** from an ordered to a disordered state with a higher degree of freedom during phase transitions. This DSC-derived phase-transition behavior is consistent with that of $[TMAEA]Pb_2Cl_6$ reported by Zhang *et al.*,[50] suggesting that **1** undergoes an isostructural phase transition followed by a ferroelectric phase transition.

Crystal structure analysis

Single-crystal X-ray diffraction experiments were performed at different temperatures to elucidate the phase-transition mechanism of **1**. In the low-temperature phase (LTP), **1** crystallizes in the chiral space group $P2_1$, with detailed unit-cell parameters provided in Table S2. The asymmetric unit of the LTP

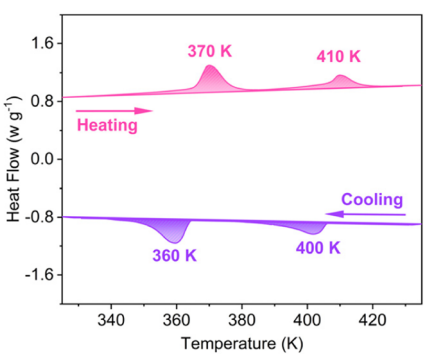

Fig. 1 DSC curves from a heating–cooling cycle of **1**.

comprises an anionic $\{K_2[Nd(NO_3)_6]_2\}^{4-}$ framework accompanied by ordered *R*M3HQ cations (Fig. 2a). This anionic assembly is constructed *via* two distinct coordination modes: (i) each Nd^{3+} center is chelated by six nitrate ligands to form a distorted $Nd(NO_3)_6$ octahedron; and (ii) each K^+ acts as a dual-coordination linker, bridging two oxygen atoms of the *R*M3HQ cation and donor oxygen atoms from nitrate groups of adjacent $[Nd(NO_3)_6]$ units. Notably, K^+ displays two bridging modes toward nitrate oxygen atoms: μ_2-κ^3(O, O′, O″) and μ_2-κ^2(O, O′). These intricate linkage patterns collectively construct a 3D framework (Fig. 2b). The packing diagram further reveals that the metal nodes are interconnected through a combination of boat-shaped and chair-shaped hexahedral units, forming a highly interconnected topological network that underpins the thermal stability and phase-transition behavior exhibited by **1** (Fig. 2c).

Unlike conventional 3D bimetallic halide perovskites, **1** features a hybrid of face- and corner-sharing linkages between K^+/Nd^{3+}-centered polyhedra. Specifically, each $[Nd(NO_3)_6]$ octahedron connects with an adjacent KO_8 dodecahedron *via* face sharing to form a bimetallic dimer, and these dimers are further linked to adjacent dimers through corner sharing (Fig. 2d). Topological analysis *via* the Topos program reveals that the K^+/Nd^{3+} 3D framework possesses a 4-connected LON topology with the vertex symbol 6^6. At 390 K, **1** retains the monoclinic space group $P2_1$, confirming the occurrence of an isostructural phase transition. The primary structural change is manifested in the progressive disordering of nitrate ligands: two of the six NO_3^- groups in each $[Nd(NO_3)_6]$ unit adopt a two-fold disordered configuration, while the thermal vibrations of guest cations are intensified. Despite these dynamic perturbations, the local coordination geometry remains well-defined: the Nd–O bond lengths range from 2.54 to 2.61 Å, K–O bond distances range from 2.84 to 3.16 Å, and O–K–O bond angles range from 27.3° to 159.8°. These structural parameters confirm that the inorganic $\{K_2[Nd(NO_3)_6]_2\}^{4-}$ framework preserves its structural integrity upon heating, thus providing a stable scaffold for the order–disorder transitions of nitrate and organic moieties (Fig. 2d).

Upon heating to 428 K, **1** transforms into a high-temperature phase (HTP), crystallizing in the hexagonal space group $P6_322$. This transition corresponds to a ferroelectric phase change, which is primarily characterized by a pronounced increase in dynamic disorder: all nitrate ligands in the $[Nd(NO_3)_6]$ units adopt a twofold disordered configuration, while the guest cations exhibit threefold disorder. Despite the substantially enhanced motional freedom of these moieties at elevated temperatures, the inorganic $\{K_2[Nd(NO_3)_6]_2\}^{4-}$ framework retains structural integrity (Fig. 2d). Variable-temperature PXRD measurements were further performed to elucidate the phase transition behavior of **1** (Fig. S4). A comparison of the diffraction patterns between the LTP and ITP shows no diffraction peak disappearance, indicating the absence of symmetry breaking and thus confirming an isostructural phase transition at this stage. Upon further heating to the HTP, a notable reduction in the number of resolvable diffraction peaks is observed—this phenomenon is consistent with the structural characteristics of a higher-symmetry space group and aligns with the aforementioned single-crystal structural analysis and physical property measurements.

Hirshfeld surface analysis and two-dimensional fingerprint plots were employed to elucidate the intermolecular interaction origins of the structural stability of **1** (Fig. 3). The results reveal that O–H···O/N–H···O hydrogen bonds dominate the crystal interactions (≈65.8%), followed by H···H van der Waals interactions (≈25.5%). Sharp peaks and high-density regions concentrated at low d_e and d_i values in the fingerprint plots (Fig. 3b–d) confirm the strong directionality and high density of the hydrogen-bond network. This network is primarily formed from multidirectional linkages between hydroxyl/amino hydrogen atoms of the organic *R*M3HQ cations and nitrate oxygen atoms in the inorganic framework; it interpenetrates with the K^+/Nd^{3+} coordination network to construct a robust 3D interaction network. Upon heating, the hydrogen-bond network exhibits dynamic behavior without complete

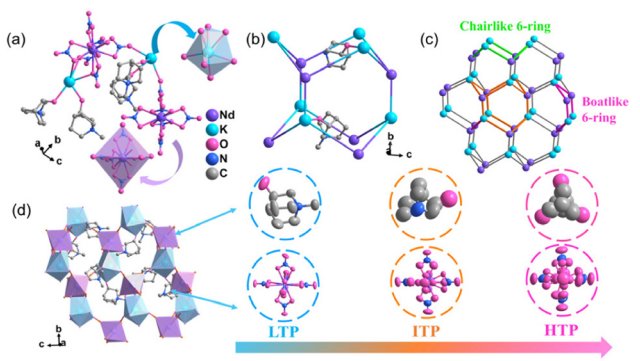

Fig. 2 (a) The minimum asymmetric unit of **1**. (b) The three-dimensional metal framework diagram of **1**. For clarity, ligands were omitted while metal atoms were retained. (c) The topological diagram of **1**. For clarity, ligands were omitted while metal atoms were retained. (d) The stacking diagram of **1** and the structural changes of *R*M3HQ and Nd $(NO_3)_6$ between the LTP, ITP, and HTP.

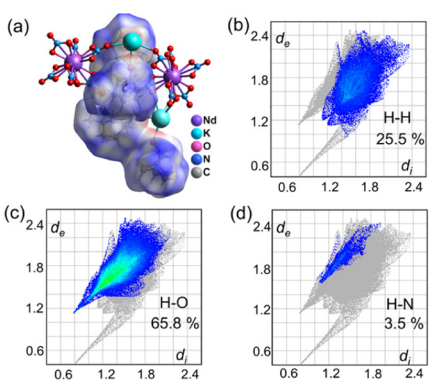

Fig. 3 Analysis of the Hirshfeld surface of **1**. (a) A schematic plot of the surface of **1**. (b–d) The fingerprint plots for **1**, displayed against the background of all intermolecular contacts, highlighting the H···H, H–O and H–N hydrogen-bonding interactions, respectively.

dissociation, introducing an additional cooperative energy barrier that suppresses inorganic framework distortion and organic cation disordering, thus elevating the phase-transition temperature above 410 K.

Ferroelectricity and ferroelasticity

Variable-temperature second-harmonic generation (VT-SHG) measurements were conducted to probe symmetry evolution during phase transitions. In its low-temperature phase, **1** exhibits a SHG response with an intensity approximately 0.25 times that of the KDP reference (Fig. S5). The SHG intensity slightly attenuates near T_1 (≈370 K), drops significantly near T_2 (≈410 K), and eventually falls to a negligible level (Fig. 4a). This trend is consistent with the crystal structure phase transition pathway (Fig. 1), further confirming the reversibility of the phase transition process. SHG switching cycling test results were further obtained for **1** (Fig. S6), which demonstrate that the SHG signal exhibits good reversibility and stability over multiple cycles. To clarify the dielectric response characteristics associated with the phase transitions, we measured the dielectric constant of **1** at multiple frequencies over the temperature range of 310–440 K (Fig. 4b and Fig. S7). Consistent with the symmetry evolution and phase transition behavior revealed by VT-SHG measurements, the real part of the dielectric constant (ε') exhibits reversible changes during both heating and cooling at 1 MHz, with two distinct dielectric anomalies observed near the corresponding phase transition temperatures (T_1 ≈ 370 K and T_2 ≈ 410 K, Fig. 4b). Thermal hysteresis of ~10 K is observed between the cooling and heating curves, which is consistent with the DSC results and further confirms the structural reversibility of the phase transitions (Fig. 1).

Polarization–electric field (*P*–*E*) hysteresis loop measurements were performed on the (010) crystallographic face of a single crystal of **1** to characterize its ferroelectric switching behavior (Fig. 4c). At 293 K, the material displays a typical ferroelectric hysteresis loop with saturation polarization (P_s) ≈ 2.5 μC cm^{-2} and a coercive field (E_c) of 95 kV cm^{-1}. Upon heating to 392 K, P_s increases to ~2.7 μC cm^{-2}, while E_c decreases significantly to 75 kV cm^{-1}. The well-defined open *P*–*E* loop confirms the intrinsic ferroelectric nature of **1**. The temperature dependence of P_s and E_c originates from thermally activated domain dynamics and a reduced energy barrier for polarization switching, and such temperature-sensitive ferroelectric responses endow **1** with great potential for application in thermally tunable ferroelectric devices. Among newly developed hybrid rare-earth double perovskites, **1** exhibits a notably high Curie temperature (T_c). This represents a high T_c value within this specific system and falls in the moderate T_c range based on reports of ferroelectrics across diverse structural systems (Fig. 4d and Table S3).[6,10,15,40,42–44,50–62]

Variable-temperature single-crystal X-ray diffraction confirms the symmetry evolution from $P2_1$ to $P6_322$ during the ITP-to-HTP transition, a structural characteristic closely associated with ferroelasticity. Complementary to this structural evidence, *in situ* polarized light microscopy was employed to directly visualize the ferroelastic domain evolution. Characteristic striped ferroelastic domains emerge progressively on the crystal surface upon cooling from 420 K to 380 K, marking the onset of the ferroelastic phase (Fig. 5). These domains vanish completely upon reheating to 420 K, with the crystal recovering its higher-symmetry state. Reversible domain formation and disappearance during repeated thermal cycling provide direct microscopic evidence for the ferroelastic phase transition, and these observations further confirm the coexistence of ferroelectricity and ferroelasticity in **1**, establishing it as a promising candidate for advanced multiferroic device applications.

Semiconductor properties

Compound **1** was further characterized by UV-vis absorption spectroscopy, and first-principles calculations based on

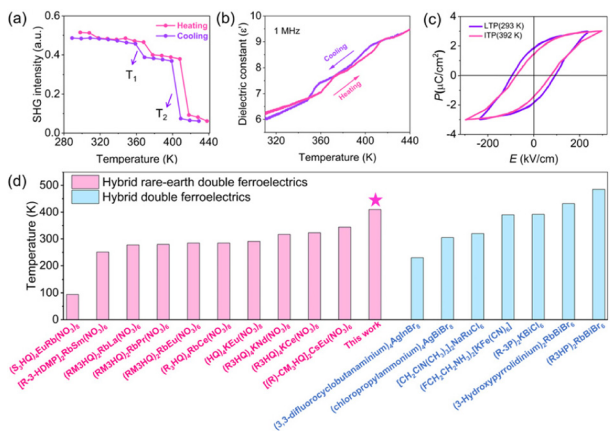

Fig. 4 (a) The temperature dependence of the SHG intensity of **1** during a heating–cooling cycle. (b) The temperature dependence of the real part of the dielectric constant of **1** at 1 MHz during a heating–cooling cycle. (c) *P*–*E* hysteresis loops of **1** measured along the *b*-axis at 293 K and 392 K. (d) A comparison of the phase transition temperature of **1** with those of representative organic, inorganic, hybrid, and rare-earth hybrid double perovskite ferroelectric materials.

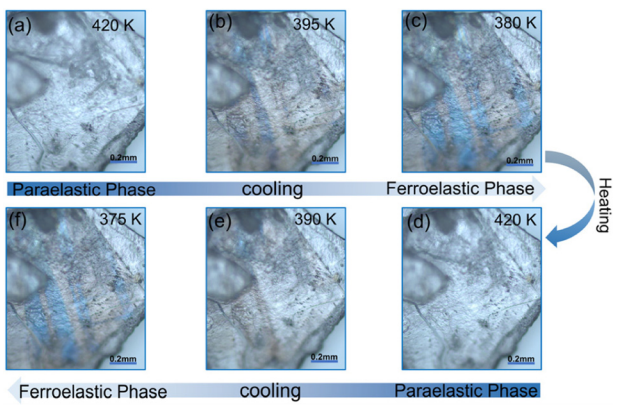

Fig. 5 The reversible evolution of ferroelastic domains under polarized light microscopy during thermal cycling. (a–c) Domain formation during initial cooling. (c and d) Domain disappearance upon heating. (d–f) Domain reappearance during subsequent cooling.

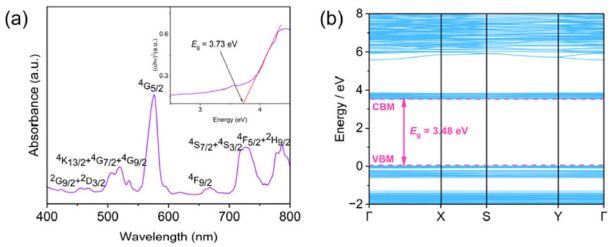

Fig. 6 (a) The solid-state UV-vis absorption spectrum. The inset shows the fitting of the absorption spectrum for band gap determination. (b) The calculated band structure of **1**.

density functional theory (DFT) were performed to determine its band structure characteristics. The UV-vis diffuse reflectance spectrum shows that the highest absorption peak of the compound is located at 576 nm. The optical band gap was determined using the modified Tauc equation, which is expressed as follows:

$$[h\nu F(R_\infty)]^{1/2} = A(h\nu - E_g)$$

where h is Planck's constant, ν is the photon frequency, $F(R_\infty)$ is the Kubelka–Munk function, and A is the proportionality constant. Using this method, the optical band gap (E_g) of **1** was determined to be 3.73 eV (Fig. 6a). Meanwhile, theoretical calculations were carried out to further verify the band gap characteristics. The results indicate that the compound exhibits indirect band gap semiconductor behavior, with a theoretical band gap value of 3.48 eV (Fig. 6b). The experimental and theoretical band gap values are in good agreement, confirming the accuracy of the structural model derived from single-crystal analysis.

Conclusions

In this work, we successfully synthesized a rare-earth/alkali–metal hybrid double perovskite featuring an unusual three-dimensional topological structure, which undergoes two consecutive phase transitions and exhibits the coexistence of ferroelectricity and ferroelasticity. This study not only verifies that rational molecular design and structural modulation can achieve high-temperature multiferroicity in rare-earth hybrid systems but also reveals an order–disorder synergistic transition mechanism that provides an important design strategy and material platform for the future development of novel smart materials with multiple responsive functionalities.

Author contributions

Li-Ping Wang and Chang-Chun Fan: measurements, formal analysis, investigation, writing-original draft; Zheng-Hui Hu and Hong-Fei Zhao: single-crystal analysis, structural depiction, ferroelastic domain measurements and hysteresis loop measurements; Chang-Chun Fan and Chao Shi: funding acquisition; Jian-Rong Li and Chao Shi: conceived the idea of the work, formal analysis, investigation, visualization and writing-review & editing draft.

Conflicts of interest

The authors declare no conflicts of interest.

Data availability

All data included in this study are available upon request by contacting the corresponding author. Supplementary information (SI) is available. See DOI: **https://doi.org/10.1039/d6qi00400h.**

CCDC 2445289–2445291 contain the supplementary crystallographic data for this paper.[63a–c]

Acknowledgements

This work was supported by the National Natural Science Foundation of China (No. 22175079), the Natural Science Foundation of Jiangxi Province (No. 20225BCJ23006 and 20224ACB204002), the Talent Introduction Project of Jinling Institute of Technology (JIT-B-202414) and the Open Project Program of Jiangxi Province Key Laboratory of Functional Crystalline Materials Chemistry, Jiangxi University of Science and Technology (2024SSY05161).

References

1 M. Fiebig, T. Lottermoser, D. Meier and M. Trassin, The evolution of multiferroics, *Nat. Rev. Mater.*, 2016, **1**, 16046–16059.
2 H.-Y. Zhang, Y.-Y. Tang, Z.-X. Gu, P. Wang, X.-G. Chen, Q. Jiang, N. Gu, S.-Q. Ren and R.-G. Xiong, Biodegradable ferroelectric molecular crystal with large piezoelectric response, *Science*, 2024, **383**, 1492–1498.
3 X.-X. Chen, X.-Y. Zhang, D.-X. Liu, R.-K. Huang, S.-S. Wang, L.-Q. Xiong, W.-X. Zhang and X.-M. Chen, Room-temperature ferroelectric and ferroelastic orders coexisting in a new tetrafluoroborate-based perovskite, *Chem. Sci.*, 2021, **12**, 8713–8721.
4 Y.-Y. Gao, M.-Y. Gao and Y.-R. Lu, Two-dimensional multiferroics, *Nanoscale*, 2021, **13**, 19324–19340.
5 E. Hassanpour, M. C. Weber, Y. Zemp, L. Kuerten, A. Bortis, Y. Tokunaga, Y. Taguchi, Y. Tokura, A. Cano, T. Lottermoser and M. Fiebig, Interconversion of multiferroic domains and domain walls, *Nat. Commun.*, 2021, **12**, 2755–2760.
6 H.-K. Li, L.-P. Wang, N. Wang, Z.-Z. Cui, L.-L. Zou, L.-P. Miao, H.-Y. Ye and C. Shi, Hybrid rare-earth double perovskite ferroic with near-infrared light-emitting property, *Chem. Mater.*, 2024, **36**, 8846–8853.

7 M. M. Lun, F. L. Zhou, D. W. Fu and Q. Ye, Multi-functional hybrid perovskites with triple-channel switches and optical properties, *J. Mater. Chem. C*, 2022, **10**, 11371–11378.
8 M. Maczka, A. Nowok, J. K. Zareba, D. Stefanska, A. Gagor, M. Trzebiatowska and A. Sieradzki, Near-Infrared Phosphorescent Hybrid Organic-Inorganic Perovskite with High-Contrast Dielectric and Third-Order Nonlinear Optical Switching Functionalities, *ACS Appl. Mater. Interfaces*, 2022, **14**, 1460–1471.
9 M. Maczka, J. K. Zareba, A. Gagor, K. Fedoruk-Piskorska, D. Stefanska, D. Drozdowski, M. Ptak and A. Sieradzki, Multi-Noncentrosymmetric Polar Order in 2D Hybrid Lead Chloride with Broadband Emission and High-Temperature Second-Harmonic Generation Switching, *ACS Appl. Mater. Interfaces*, 2024, **16**, 60564–60575.
10 M. Rok, A. Cizman, B. Zarychta, J. K. Zareba, M. Trzebiatowska, M. Maczka, A. Stroppa, S. R. Yuan, A. E. Phillips and G. Bator, Cyano-bridged perovskite $(CH_3)_3NOH_2KM(CN)_6$, M: Fe(iii), and Co(iii) for high-temperature multi-axial ferroelectric applications with enhanced thermal and nonlinear optical performance, *J. Mater. Chem. C*, 2020, **8**, 17491–17501.
11 M. Wojciechowska, A. Gagor, A. Piecha-Bisiorek, R. Jakubas, A. Cizman, J. K. Zareba, M. Nyk, P. Zielinski, W. Medycki and A. Bil, Ferroelectricity and Ferroelasticity in Organic Inorganic Hybrid $(Pyrrolidinium)_3Sb_2CL_9$, *Chem. Mater.*, 2018, **30**, 4597–4608.
12 F. Orlandi, D. Delmonte, G. Calestani, E. Cavalli, E. Gilioli, V. V. Shvartsman, P. Graziosi, S. Rampino, G. Spaggiari, C. Liu, W. Ren, S. Picozzi, M. Solzi, M. Casappa and F. Mezzadri, γ-$BaFe_2O_4$: a fresh playground for room temperature multiferroicity, *Nat. Commun.*, 2022, **13**, 7968–7977.
13 A. O. Polyakov, A. H. Arkenbout, J. Baas, G. R. Blake, A. Meetsma, A. Caretta, P. H. M. van Loosdrecht and T. T. M. Palstra, Coexisting ferromagnetic and ferroelectric order in a $CuCl_4$-based organic-inorganic hybrid, *Chem. Mater.*, 2011, **24**, 133–139.
14 L. Ponet, S. Artyukhin, T. Kain, J. Wettstein, A. Pimenov, A. Shuvaev, X. Wang, S. W. Cheong, M. Mostovoy and A. Pimenov, Topologically protected magnetoelectric switching in a multiferroic, *Nature*, 2022, **607**, 81–85.
15 L. He, P.-P. Shi, L. Zhou, Z.-B. Liu, W. Zhang and Q. Ye, Coexisting ferroelectric and ferroelastic orders in rare 3D homochiral hybrid bimetal halides, *Chem. Mater.*, 2021, **33**, 6233–6239.
16 L.-P. Miao, L.-L. Chu, X.-B. Han, B.-D. Liang, C.-Y. Chai, C.-C. Fan, X.-X. Wang, Y.-F. Yao and W. Zhang, A ferroelastic molecular rotor crystal showing inverse temperature symmetry breaking, *Inorg. Chem. Front.*, 2021, **8**, 2809–2816.
17 D.-X. Liu, Z.-H. Yu, X.-X. Chen, W.-X. Zhang and X.-M. Chen, Crystal structures and phase transitions in two new hybrid crystals: $(Me_3NCH_2CH_2X)_4Ni(NCS)_6$ (X = Cl and Br), *Chin. Chem. Lett.*, 2023, **34**, 107310.
18 H.-Y. Liu, H.-Y. Zhang, X.-G. Chen and R.-G. Xiong, Molecular design principles for ferroelectrics: Ferroelectrochemistry, *J. Am. Chem. Soc.*, 2020, **142**, 15205–15218.
19 Z.-Y. Yu, G.-F. Li, Z.-K. Xu, L.-P. Long, Y. Qin, Z.-Y. Du and Z.-X. Wang, Enantiomeric organic amine-borane adduct crystals with room-temperature multi-channel switches, *Chin. J. Struct. Chem.*, 2025, **44**, 100715.
20 D.-X. Feng, Y. Mu, J. Li, S.-D. Han, J.-H. Li, H.-L. Sun, M. Pan, J.-X. Hu and G.-M. Wang, Light-induced electron transfer toward on/off room temperature phosphorescence in two photochromic coordination polymers, *Adv. Funct. Mater.*, 2023, **33**, 2305796–2305803.
21 R. Zhao and H. Yang, Oxygen vacancies induced tuning effect on physical properties of multiferroic perovskite oxide thin films, *Acta Phys. Sin.*, 2018, **67**, 156101.
22 D.-F. Zhang, L.-L. Zheng, Y.-Z. Ma, S.-F. Wang, Z.-Q. Bian, C.-H. Huang, Q.-H. Gong and L.-X. Xiao, Factors influencing the stability of perovskite solar cells, *Acta Phys. Sin.*, 2015, **64**, 038803.
23 C.-C. Fan, C.-D. Liu, B.-D. Liang, W. Wang, M.-L. Jin, C.-Y. Chai, C.-Q. Jing, T.-Y. Ju, X.-B. Han and W. Zhang, Tuning ferroelectric phase transition temperature by enantiomer fraction, *Nat. Commun.*, 2024, **15**, 1464–1472.
24 A. Zhang, C.-X. Zhang, C.-M. Zhang, Y.-M. Tian, J. Yan and T. Meng, Effects of CH_3NH_3 polymer formation on performance of organic-inorganic hybrid perovskite solar cell, *Acta Phys. Sin.*, 2021, **70**, 168801.
25 Z.-S. Yang, W.-F. Ke, Y.-X. Wang, L.-Q. Huang, P.-C. Guo and H. Zhu, Preparation and characterization of a novel hybrid perovskite $(HOC_2H_4NH_3)_2CuCl_4$, *J. Inorg. Mater.*, 2017, **32**, 1063–1067.
26 Y.-F. Zhang, H. Wang, Y. Liu and C. Li, Aromatic bromination with hydrogen production on organic-inorganic hybrid perovskite-based photocatalysts under visible light irradiation, *Chin. J. Catal.*, 2022, **43**, 1805–1811.
27 Z.-L. Xiao, H.-Z. Chen, M.-M. Shi, G. Wu, R.-J. Zhou, Z.-S. Yang, M. Wang and B.-Z. Tang, Preparation and characterization of organic-inorganic hybrid perovskite $(C_4H_9NH_3)_2CuCl_4$, *Mater. Sci. Eng., B*, 2005, **117**, 313–316.
28 Q. Song, C. A. Occhialini, E. Ergecen, B. Ilyas, D. Amoroso, P. Barone, J. Kapeghian, K. Watanabe, T. Taniguchi, A. S. Botana, S. Picozzi, N. Gedik and R. Comin, Evidence for a single-layer van der Waals multiferroic, *Nature*, 2022, **602**, 601–605.
29 K. Taniguchi, M. Nishio, N. Abe, P. J. Huang, S. Kimura, T. H. Arima and H. Miyasaka, Magneto-electric directional anisotropy in polar soft ferromagnets of two-dimensional organic-inorganic hybrid perovskites, *Angew. Chem., Int. Ed.*, 2021, **60**, 14350–14354.
30 M.-X. Wu and M.-R. Li, Multiferroic properties of exotic double perovskite $A_2BB'O_6$, *Acta Phys. Sin.*, 2018, **67**, 157510.
31 X.-H. Xu, F.-T. Huang, K. Du and S.-W. Cheong, Multifunctionality of $Li_2SrNb_2O_7$: memristivity, tunable rectification, ferroelasticity, and ferroelectricity, *Adv. Mater.*, 2022, **34**, 2206022.
32 Y.-L. Yang, J.-Y. Ji, J.-S. Feng, S.-Y. Chen, L. Bellaiche and H.-J. Xiang, Two-dimensional organic-inorganic room-

temperature multiferroics, *J. Am. Chem. Soc.*, 2022, **144**, 14907–14914.
33 T.-Y. Ju, C.-C. Fan, B.-D. Liang, C.-D. Liu, M.-L. Jin, C.-Y. Chai and W. Zhang, Chirality triggered biferroicity in a 3D rubidium based perovskite, *Adv. Funct. Mater.*, 2024, **34**, 2316747.
34 L. Zhou, X. Wang, H.-M. Zhang, X.-D. Shen, S. Dong and Y.-W. Long, High pressure synthesis and physical properties of multiferroic materials with multiply-ordered perovskite structure, *Acta Phys. Sin.*, 2018, **67**, 157505.
35 C.-C. Fan, W.-N. Wang, Z.-M. Gu, J. Xu, W. Wang, C.-D. Liu and C. Shi, Stable 3D lead bromide hybrid ferroelectric semiconductor enabled by halogen-substitution-induced confinement effect, *Inorg. Chem. Commun.*, 2026, **183**, 115735.
36 T. Zhang, K. Xu, J. Li, L. He, D.-W. Fu, Q. Ye and R.-G. Xiong, Ferroelectric hybrid organic-inorganic perovskites and their structural and functional diversity, *Natl. Sci. Rev.*, 2023, **10**, nwac240.
37 C.-M. Ji, S.-S. Wang, L.-N. Li, Z.-H. Sun, M.-C. Hong and J.-H. Luo, The first 2D hybrid perovskite ferroelectric showing broadband white-light emission with high color rendering index, *Adv. Funct. Mater.*, 2019, **29**, 1805038.
38 H. Peng, Q. Liu, Y.-H. Liu, Y.-Z. Lu and W.-Q. Liao, A chiral lead-free tin(IV)-based halide organic-inorganic semiconductor with dielectric switching and phase transition, *Chin. Chem. Lett.*, 2023, **34**, 107980.
39 Z. Chen, Y.-Y. He, Y. Zhang and X.-M. Zhang, Ultraviolet-visible-near-infrared photoresponses realized in a polar Dion-Jacobson hybrid perovskite through light-induced pyroelectric effects, *Chem. Mater.*, 2023, **35**, 8192–8202.
40 C. Shi, L. Ye, Z.-X. Gong, J.-J. Ma, Q.-W. Wang, J.-Y. Jiang, M.-M. Hua, C.-F. Wang, H. Yu, Y. Zhang and H.-Y. Ye, Two-dimensional organic-inorganic hybrid rare-earth double perovskite ferroelectrics, *J. Am. Chem. Soc.*, 2020, **142**, 545–551.
41 C.-C. Fan, C.-D. Liu, B.-D. Liang, W. Wang, Y.-H. Zhao, C.-L. Hu, B.-X. Li and W.-Q. Liang, Record second-harmonic generation in a lead-free 2D hybrid halide perovskite, *Laser Photonics Rev.*, 2026, **20**, e01607.
42 Z.-B. Hu, C.-F. Wang, T.-T. Sha, C. Shi, L. Ye, H.-Y. Ye, Y. Song, Y.-M. You and Y. Zhang, An effective strategy of introducing chirality to achieve multifunctionality in rare-earth double perovskite ferroelectrics, *Small Methods*, 2022, 2200421.
43 Q.-Q. Jia, H.-F. Lu, J.-Q. Luo, Y.-Y. Zhang, H.-F. Ni, F.-W. Zhang, J. Wang, D.-W. Fu, C.-F. Wang and Y. Zhang, Organic-inorganic rare-earth double perovskite ferroelectric with large piezoelectric response and ferroelasticity for flexible composite energy harvesters, *Small*, 2024, **20**, 2306989.
44 M.-L. Ren, Z.-J. Xu, H.-K. Li, Z.-A. Qiu, L.-H. Shen, X. Zhang, C. Shi, N. Wang, H.-Y. Ye and L.-P. Miao, H/OH substitution, construction of K–O coordinated bonds and introduction of homochirality for the design of a 3D hybrid double perovskite multiferroic, *Inorg. Chem. Front.*, 2025, **12**, 4623–4628.
45 J. Ding and Q. Yan, Progress in organic-inorganic hybrid halide perovskite single crystal: growth techniques and applications, *Sci. China Mater.*, 2017, **60**, 1063–1078.
46 M. Manzi, G. Pica, M. De Bastiani, S. Kundu, G. Grancini and M. I. Saidaminov, Ferroelectricity in hybrid perovskites, *J. Phys. Chem. Lett.*, 2023, **14**, 3535–3552.
47 C.-C. Fan, C.-D. Liu, B.-D. Liang, T.-Y. Ju, W. Wang, M.-L. Jin, C.-Y. Chai and W. Zhang, Chiral three-dimensional organic-inorganic lead iodide hybrid semiconductors, *Chem. Sci.*, 2024, **15**, 11374–11381.
48 Y.-Y. Tang, Y.-H. Liu, H. Peng, B.-B. Deng, T.-T. Cheng and Y.-T. Hu, Three-dimensional lead bromide hybrid ferroelectric realized by lattice expansion, *J. Am. Chem. Soc.*, 2020, **142**, 19698–19704.
49 W. Wang, C.-D. Liu, C.-C. Fan and W. Zhang, A three-dimensional lead iodide perovskite analogy featuring hydrogen-bonded dual monovalent cations, *Chem. Sci.*, 2024, **15**, 18455–18462.
50 H.-Y. Zhang, X.-J. Song, H. Cheng, Y.-L. Zeng, Y. Zhang, P.-F. Li, W.-Q. Liao and R.-G. Xiong, A three-dimensional lead halide perovskite-related ferroelectric, *J. Am. Chem. Soc.*, 2020, **142**, 4604–4608.
51 C. Higashimura, G. Yumoto, T. Yamada, T. Nakamura, F. Harata, H. Hirori, A. Wakamiya and Y. Kanemitsu, Spontaneous polarization induced optical responses in a two-dimensional ferroelectric halide perovskite, *J. Phys. Chem. Lett.*, 2023, **14**, 8360–8366.
52 C. Shi, J.-J. Ma, J.-Y. Jiang, M.-M. Hua, Q. Xu, H. Yu, Y. Zhang and H.-Y. Ye, Large piezoelectric response in hybrid rare-earth double perovskite relaxor ferroelectrics, *J. Am. Chem. Soc.*, 2020, **142**, 9634–9641.
53 C.-F. Wang, C. Shi, A.-Y. Zheng, Y.-L. Wu, L. Ye, N. Wang, H.-Y. Ye, M.-G. Ju, P.-F. Duan, J.-L. Wang and Y. Zhang, Achieving circularly polarized luminescence and large piezoelectric response in hybrid rare-earth double perovskite by a chirality induction strategy, *Mater. Horiz.*, 2022, **9**, 2450–2459.
54 L. He, K. Xu, P.-P. Shi, Z.-B. Liu, W. Zhang and Q. Ye, A rare 3D hybrid bimetal halide ferroelectric: $(3\text{-Hydroxypyrrolidinium})_2RbBiBr_6$, *Sci. China Mater.*, 2022, **65**, 2879–2883.
55 D.-F. Li, F. Guo, X.-L. He, Y.-Z. Wu, X.-H. Deng, K.-P. Yang, Y. Sui and Y.-X. Li, A layered hybrid rare-earth double perovskite with two continuous reversible phase transitions induced by unusual two driving gears of fan-like rotation movements, *CrystEngComm*, 2022, **24**, 8496–8502.
56 N. Wang, Z.-J. Xu, H.-F. Ni, W. Luo, H.-K. Li, M.-L. Ren, C. Shi, H.-Y. Ye, X.-B. Fu, Y. Zhang and L.-P. Miao, Molecular engineering regulation achieving out-of-plane polarization in rare-earth hybrid double perovskites for ferroelectrics and circularly polarized luminescence, *Angew. Chem., Int. Ed.*, 2024, **63**, e202409796.
57 C.-F. Wang, Y. Yang, Y. Hu, C. Ma, H.-F. Ni, P.-G. Liu, H.-F. Lu, Z.-X. Zhang, J.-L. Wang, Y.-J. Zhang, D.-W. Fu, K. Zhao and Y. Zhang, Exploring aqueous solution-processed pseudohalide rare-earth double perovskite ferroelec-

trics toward X-ray detection with high sensitivity, *Angew. Chem., Int. Ed.*, 2024, **63**, e202413726.
58 Y.-T. Li, X. Sun, X. Yin, H. Cai and Z.-H. Wei, Reversible phase transition, dielectric and fluorescent properties of chiral 3D double perovskites, *J. Mol. Struct.*, 2026, **1351**, 144320.
59 W.-Q. Guo, X.-T. Liu, S.-G. Han, Y. Liu, Z.-Y. Xu, M.-C. Hong, J.-H. Luo and Z.-H. Sun, Room-temperature ferroelectric material composed of a two-dimensional metal halide double perovskite for X-ray detection, *Angew. Chem., Int. Ed.*, 2020, **59**, 13879–13884.
60 M.-L. Ren, S.-F. Song, Z.-J. Xu, H.-K. Li, Z.-A. Qiu, L.-H. Shen, X. Zhang, C. Shi, N. Wang, H.-Y. Ye and L.-P. Miao, F-Substitution for achieving multiferroicity in In(III)-based two-dimensional organic-inorganic hybrid halogen double perovskites, *Cryst. Growth Des.*, 2025, **25**, 6803–6809.
61 Z.-J. Xu, H.-K. Li, M.-L. Ren, L.-H. Shen, X. Zhang, Z.-A. Qiu, C. Shi, L.-D. Yu, N. Wang, H.-Y. Ye and L.-P. Miao, Long-range ferroelectric order regulated by Cl–Cl halogen bonding in a 1D Ru-based hybrid double perovskite, *Cryst. Growth Des.*, 2025, **25**, 1682–1687.
62 L.-Y. Ji, J.-S. Zhou, S.-Y. Liu, Y. Qin, H.-P. Lv and X.-G. Chen, Effective enhancement of mechanical properties via H/F substitution in 3D cyanide hybrid perovskites, *Chem. Commun.*, 2025, **61**, 13165–13168.
63 (*a*) CCDC 2445289: Experimental Crystal Structure Determination, 2026, DOI: **10.5517/ccdc.csd.cc2n2j9l**; (*b*) CCDC 2445290: Experimental Crystal Structure Determination, 2026, DOI: **10.5517/ccdc.csd.cc2n2jbm**; (*c*) CCDC 2445291: Experimental Crystal Structure Determination, 2026, DOI: **10.5517/ccdc.csd.cc2n2jcn**.